Advances in Geo-Energy Research

Vol. 17, No. 2, p. 135-148, 2025

Original article

Non-monotonic evolution and spatial reorganization mechanism of thermally induced micro-damage in sandstone

Haifeng Yan[1], Tingqiang Zhou[1]*, Xiaoyi Zhou[1]*, Xuyang Liu[2], Xin Tang[1,3]

[1]*School of Civil Engineering, Chongqing Three Gorges University, Chongqing 404199, P. R. China*

[2]*School of Engineering and Applied Science, University of Pennsylvania, Philadelphia, PA 19104, USA*

[3]*Chongqing Three Gorges Reservoir Bank Slope and Engineering Structure Disaster Prevention and Control Engineering Technology Research Center, Chongqing 404199, P. R. China*

Keywords:
Sandstone
thermal treatment
heterogeneity
atomic force microscopy
spatial autocorrelation analysis

Cited as:
Yan, H., Zhou, T., Zhou, X., Liu, X., Tang, X. Non-monotonic evolution and spatial reorganization mechanism of thermally induced micro-damage in sandstone. Advances in Geo-Energy Research, 2025, 17(2): 135-148.
https://doi.org/10.46690/ager.2025.08.05

Abstract:
This study employs transformative nanoscale-spatial methodology, which reveals the complete thermal damage evolution mechanism of sandstone from 25 to 700 °C, fundamentally challenging the conventional linear degradation paradigm. Spatial autocorrelation analysis is innovatively applied to atomic force microscopy data, establishing that thermal damage follows a non-monotonic pathway governed by spatial heterogeneity evolution rather than simple progressive weakening. Four critical temperature thresholds are identified: 200 °C marks the initiation of localized damage through expansion of weak zones with 61.4% stiffness reduction; 400 °C features unexpected transient hardening due to clay mineral dehydroxylation and pore restructuring, reaching the peak adhesion force; 500 °C represents not only increased damage but also the thermal decomposition of the 400 °C hardened structure, evidenced by maximum spatial heterogeneity and negative adhesion; and the 700 °C following quartz phase transition establishes a completely reconfigured structure with a novel "harder-in-lower-areas" pattern. Crucially, this research demonstrates that the spatial clustering of mechanical properties evolves from balanced high-low zones at 200 °C to a percolating low-stiffness network at 500 °C, establishing spatial reorganization as the governing principle of thermal damage. The findings provide a quantitative framework that can accurately predict rock behavior in geothermal systems and underground energy storage applications.

1. Introduction

In the context of applications such as geotechnical engineering, geothermal energy development and deep geological disposal, the long-term stability of rock materials in high-temperature environments is a primary factor determining engineering safety (Anderson and Rezaie, 2019; Wong et al., 2020). This is because high-temperature exposure can induce mineral phase transitions, intergranular thermal stresses, and the initiation and propagation of microcracks within the rock, typically leading to the degradation of its physical and mechanical properties (Mo et al., 2022; Guo et al., 2023). The thermally-induced damage process in sandstone, a typical porous sedimentary rock commonly encountered in engineering, is particularly complex due to its significant spatial heterogeneity (Shen et al., 2023; Gao et al., 2024; Chen et al., 2025). Therefore, it is necessary to investigate the spatial distribution of surface mechanical properties in order to refine the assessment of both engineering safety and long-term material stability.

Atomic force microscopy (AFM) (Fig. 1(a)) is an effective tool for characterizing the surface topography and mechanical

Yandy Scientific Press

*Corresponding author.
E-mail address: yanhaifeng2024@126.com (H. Yan); zhoutq1020@163.com (T. Zhou); zhouxy0520@163.com (X. Zhou); liu-xuyang@alumni.upenn.edu (X. Liu); tangxin@cumt.edu.cn (X. Tang).

Received June 25, 2025; revised July 18, 2025; accepted August 1, 2025; available online August 4, 2025.

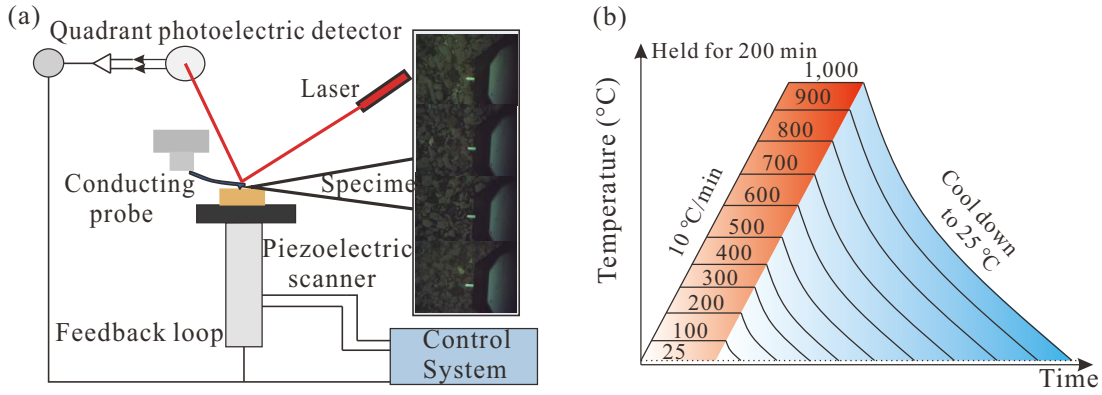

Fig. 1. Schematic diagram of (a) AFM and (b) heat treatment temperatures.

properties of heterogeneous materials such as rock at the nanoscale (Tian et al., 2024; Xie and Li, 2024; Zhu et al., 2024). Related studies have advanced the understanding of microscopic heterogeneity in rocks by quantifying the changes in surface roughness or the evolution of mechanical properties (Wu et al., 2025). However, existing analyses in data processing have predominantly focused on statistical evaluations of the average properties or on conventional image segmentation, largely overlooking the spatial organization patterns and correlations in mechanical properties (Hirono et al., 2006; Li et al., 2019; Giergiel et al., 2022; Paruchuri et al., 2024). Therefore, the questions of how damage manifests spatially-whether in clustered or dispersed distribution patterns-and how to quantitatively characterize these patterns remain largely unanswered (He et al., 2024; Wang et al., 2025). The systematic application of spatial statistical methods to translate high-resolution AFM maps into a quantitative understanding of the evolving spatial distribution of damage represents a promising avenue for research in this field.

Accordingly, this study aims to implement a multi-dimensional research framework that integrates nano-mechanical characterization with spatial statistical analysis. It utilizes AFM to acquire high-resolution maps of topography and the mechanical properties from heat-treated sandstone surfaces, and incorporates spatial autocorrelation analysis (e.g., Global Moran's I and Local Indicators of Spatial Association (LISA)) (Cliff and Ord, 1973; Anselin, 1995). This approach allows the establishment of a comprehensive analytical chain that progresses from "average property degradation" to "spatial distribution reorganization", and ultimately achieves the "evolution of the topography-mechanics coupling". This work seeks to provide a novel quantitative perspective and an analytical pathway for a deeper understanding of the damage mechanisms in sandstone under extreme environments.

2. Materials and methods

2.1 Materials and sample preparation

For the experiments, pale bluish sandstone samples were collected from the shores of the Three Gorges Reservoir in Wanzhou District, Chongqing, China. For gas adsorption tests, 11 sets of sandstone samples (approximately 2 g per set) were pulverized to 40-80 mesh according to the GB/T 21650.3-2011 national standard. Concurrently, bulk samples for AFM analysis were prepared from the same rock formation. To address the challenges related to mechanical polishing arising from the heterogeneous surface composition and the varying mineral hardness of sandstone, as well as to meet the requirements for the surface roughness of AFM, bulk specimens were cold-mounted in epoxy resin. This protective measure effectively preserved the microscopic structures of samples during subsequent mechanical polishing procedures.

All samples, in both their powdered and bulk forms, were subjected to a stepwise heat treatment protocol under ambient pressure. Starting from room temperature (25 °C, as-received control), the samples were heated to a series of target temperatures: 100, 200, 300, 400, 500, 600, 700, 800, 900, and 1,000 °C. A constant heating rate of 10 °C/min was used, and a holding time of 200 min was applied at each target temperature to ensure thermal equilibrium. Subsequently, all samples were allowed to cool naturally to room temperature within the furnace to maintain a consistent cooling rate and minimize thermal shock (Fig. 1(b)). To ensure direct comparability, the bulk samples designated for AFM analysis underwent the exact same heat treatment protocol. After cooling, all prepared samples were stored in sealed and labeled bags. For the AFM analysis, five distinct regions were tested on each sample (e.g., 25.001-25.005) to ensure the representativeness and statistical reliability of the collected data.

2.2 Gas adsorption experiments

In order to investigate the evolution of pore structure in sandstone after thermal treatment, low-temperature N_2 and CO_2 adsorption experiments were conducted. The micropore volume was determined from the CO_2 adsorption data using the Dubinin-Radushkevich model (Dubinin and Radushkevich, 1947), while the mesopore volume was calculated from the low-temperature N_2 adsorption data via the Barrett-Joyner-Halenda method (Barrett et al., 1951). To identify the critical temperatures governing pore structure evolution, a "pore weighting coefficient" (ω_{ij}) was defined. This coefficient quantifies the fractional volume of each pore class at a specific temperature and is calculated as:

$$\omega_{ij} = \frac{V_{ij}}{V_i} \tag{1}$$

where V_{ij} represents the volume of a given pore-size class at temperature T_i, while V_i represents the total pore volume at the same temperature. The temperature index i ranges from 1 (25 °C) to 11 (1,000 °C). The pore-size class index j was defined as follows: $j = 1$ for micropores (0-2 nm), $j = 2$ for small mesopores (2-20 nm), and $j = 3$ for large mesopores (20-50 nm).

2.3 AFM experiments

The surface topography and nanomechanical properties of the bulk sandstone samples were characterized using a Bruker Dimension Icon AFM system operating in Quantitative Nanomechanical Mapping mode. All AFM tests were performed under controlled ambient laboratory conditions, with the temperature actively controlled and stabilized at 25.0 °C. The nanomechanical properties of the samples were characterized using the Derjaguin-Muller-Toporov model (Derjaguin et al., 1975), wherein the relationship between force and indentation is described as:

$$F = \frac{4}{3}E^*\sqrt{R\delta^3} + F_a \tag{2}$$

where F represents the applied force, R represents the radius of curvature of the probe tip, δ denotes the indentation depth, and F_a is the adhesion force. The reduced modulus (E^*), which serves as a robust indicator of the material's elastic properties, was directly extracted by fitting the force-displacement curves to this Derjaguin-Muller-Toporov model. The definition of the reduced modulus incorporates the elastic properties of both the sample and the probe:

$$\frac{1}{E^*} = \frac{1-\nu_p^2}{E_p} + \frac{1-\nu_s^2}{E_s} \tag{3}$$

where E_s and ν_s are the Young's modulus and Poisson's ratio of the sample, respectively, and E_p and ν_p are those of the probe, respectively. Throughout this study, all subsequent analyses, including spatial statistics, were based on the calculated reduced modulus (E^*) values. All AFM tests were conducted on twenty-five independent 5 × 5 μm^2 regions, with an image resolution of 256 × 256 pixels.

2.4 Processing and analysis of AFM surface topography

From the AFM height images, several topographical parameters were calculated, including roughness parameters R_a, R_q and R_z, which quantify the average, root-mean-square, and maximum peak-to-valley height deviations, respectively, and the height distribution parameters R_s and R_k, which describe the asymmetry and sharpness of the surface topography, respectively (Chen et al., 2022; Zhou et al., 2025). Additionally, other metrics such as the Gaussian curvature (K) (Gauss, 1828) and the Euler characteristic were determined, with the latter given by the following equation:

$$K = \frac{h_{xx}h_{yy} - (h_{xy})^2}{(1+h_x^2+h_y^2)^2} \tag{4}$$

where h_x and h_y are the first-order partial derivatives representing the local slope, while h_{xx}, h_{yy}, and h_{xy} are the second-order partial derivatives describing local curvature and twisting. The sign of K indicates the local surface geometry (e.g., convex, concave, or saddle-shaped).

The Euler characteristic (χ) was determined by counting the number of peaks and pits after binarizing the image (Haralick et al., 1987). This parameter characterizes the overall topological connectivity and is calculated as:

$$\chi = N_p - N_h \tag{5}$$

where N_p denotes the number of separate connected domains (peaks), and N_h is the number of holes (valleys) completely enclosed within these domains.

2.5 Spatial autocorrelation analysis of nanomechanical properties

This study employs spatial autocorrelation analysis-specifically, Global Moran's Index and LISA-to investigate the overall spatial patterns and local clustering features of nanomechanical properties on the sample surfaces. Global Moran's Index measures the overall spatial autocorrelation of a given attribute across the entire study area (Moran, 1950), determining whether similar values (either high or low) tend to be spatially clustered, dispersed, or randomly distributed. The index I is calculated using the following formula:

$$I = \frac{N}{\sum_{i=1}^{N}\sum_{j=1}^{N} w_{ij}} \frac{\sum_{i=1}^{N}\sum_{j=1}^{N} w_{ij}(x_i-\bar{x})(x_j-\bar{x})}{\sum_{i=1}^{N}(x_i-\bar{x})^2} \tag{6}$$

where N represents the total number of pixels; x_i and x_j are the values of the mechanical property for pixels i and j, respectively; $\bar{x}$ represents the mean value of this property across all pixels; and w_{ij} is the spatial weight defining the proximity between pixel i and j.

The Local Moran's I for a spatial unit i, denoted as I_i, is calculated using the following formula (Anselin, 1995):

$$I_i = \frac{(x_i-\bar{x})}{S^2}\sum_{\substack{j=1\\ j\neq i}}^{N} W_{ij}(x_j-\bar{x}) \tag{7}$$

where x_i denotes the value of the property at location i; $\bar{x}$ represents the mean of the property across all locations; x_j represents the value at another location j; W_{ij} represents the spatial weight defining the proximity between locations i and j; and S^2 is the sample variance of the property. The analysis of local spatial autocorrelation involves assessing the statistical significance of each local index, I_i, and considering the combination of signs between a location's deviation from the mean and its spatial lag.

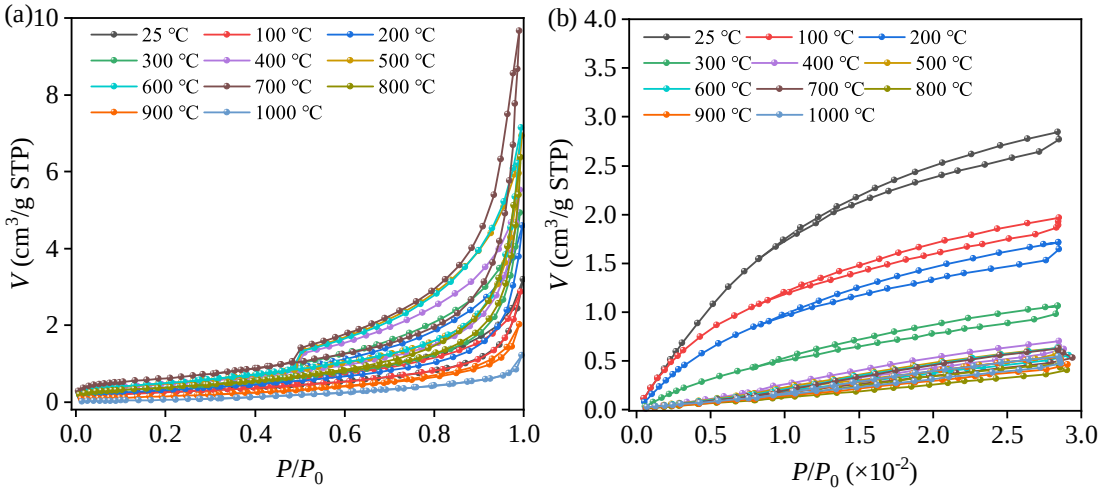

Fig. 2. Adsorption isotherms of sandstone: (a) N_2 adsorption at 77 K and (b) CO_2 adsorption at 273 K, both plotted as a function of relative pressure (P/P_0).

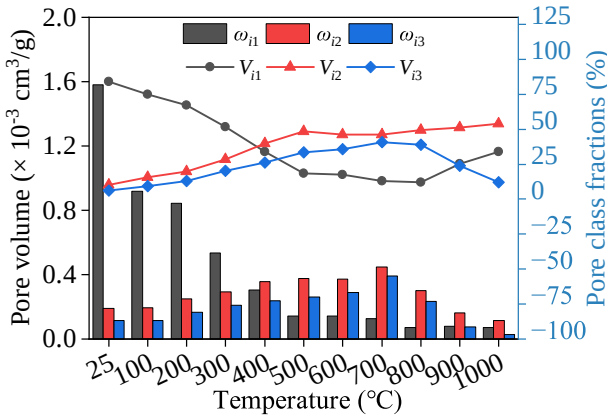

Fig. 3. Variation in pore parameters in the carbon dioxide and nitrogen gas adsorption experiments.

3. Results

3.1 Gas adsorption results and selection of critical temperatures

In order to guide the subsequent AFM investigation into the microstructural evolution of heat-treated sandstone, preliminary gas adsorption experiments were conducted to identify the critical temperatures at which significant pore structural changes occur. The analysis combined low-temperature N_2 (77 K) and CO_2 (273 K) adsorption data (Fig. 2) to characterize mesopore and micropore structures, respectively, for samples treated at various temperatures: 25, 100, 200, 300, 400, 500, 600, 700, 800, 900, and 1,000 °C.

On the basis of a comprehensive evaluation of pore structure parameters (Fig. 3), this study selected 25, 200, 400, 500, and 700 °C as the key temperatures for in-depth AFM characterization, as they represent critical stages of pore network evolution. This selection was based on the following observations. At the baseline temperature of 25 °C, the pore volume was dominated by micropores (0-2 nm), which accounted for 83.9% (pore weighting coefficient, ω_{11}), while small (2-20 nm) and large (20-50 nm) mesopores constituted 10.0% (ω_{12}) and 6.1% (ω_{13}), respectively. By 200 °C, a significant redistribution began, with ω_{31} dropping to 67.1% as ω_{32} and ω_{32} increased to 19.8% and 13.1%. This trend continued to 400 °C, where ω_{51} decreased substantially to 33.8%, compensated by a sharp rise in ω_{52} to 39.8%, while ω_{53} stabilized at 26.3%. At 500 °C, the total pore volume reached a local minimum of approximately 0.00782 cm^3/g, withω_{61} declining to 18.4% and the combined mesopore and macropore fractions growing to 48.3% and 33.2%. Finally, at 700 °C, the structure was dominated by mesopores, as ω_{82} and ω_{83} surged to 46.4% and 40.6%, collectively accounting for over 87% of the total pore volume, while ω_{81} was reduced to 13.0%. The total pore volume at this stage rebounded from its 500 °C minimum, increasing to 0.0186 cm^3/g.

3.2 Surface topological features at the key temperatures

After the selection of key temperatures based on the gas adsorption results, the corresponding heat-treated sandstone samples were characterized via AFM. This analysis aimed to directly observe the evolution of their surface micromorphology and quantify the changes in their topological features. Fig. 4 illustrates the representative AFM height maps of sandstone samples at the selected key temperatures. To characterize the topological complexity of the AFM-observed surfaces, a multi-dimensional analysis was conducted on the processed height data. The results (Fig. 5(b)) indicated that parameters describing the surface amplitude, namely, the arithmetic mean roughness (R_a), root-mean-square roughness (R_q), and maximum peak to valley height (R_z), as well as those describing the symmetry of height distribution (skewness, R_s) and sharpness (kurtosis, R_k), all evolved with temperature. To further investigate the evolution of the topological features, the Gaussian curvature (K) at the local scale, along with the Euler characteristic (χ) and fractal dimension at the global scale, were calculated. Gaussian curvature quantifies (Fig. 6) the local bending morphology at any given point ($K > 0$ indicates

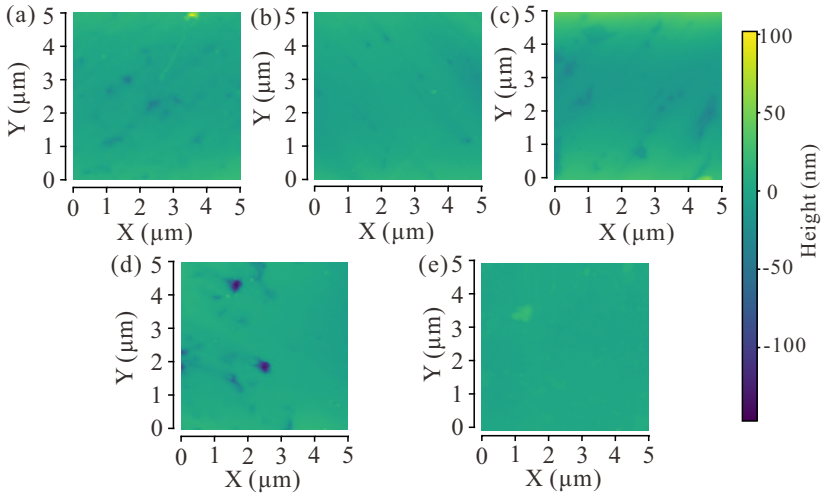

Fig. 4. AFM morphology after heat treatment: (a) 25 °C, (b) 200 °C, (c) 400 °C, (d) 500 °C and (e) 700 °C.

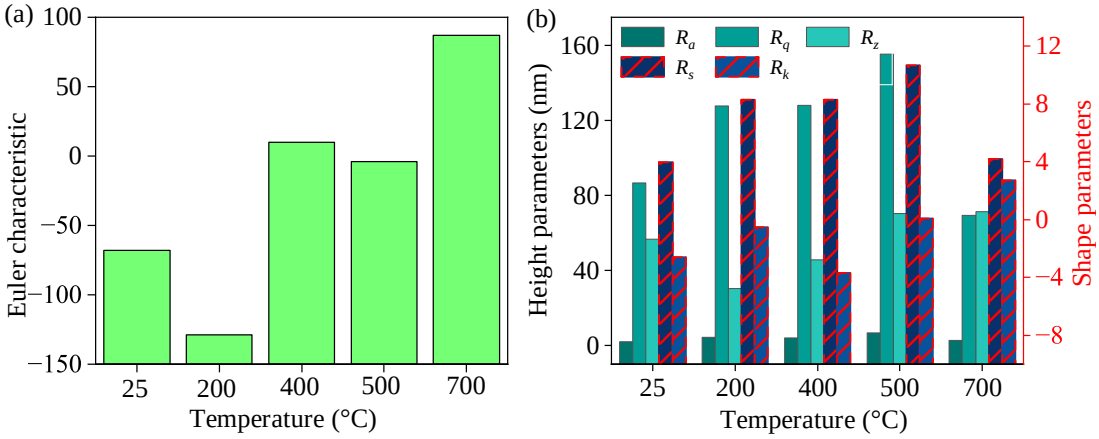

Fig. 5. Evolution of surface topological and topographical parameters with temperature. (a) Euler characteristic and (b) average surface topographical parameters.

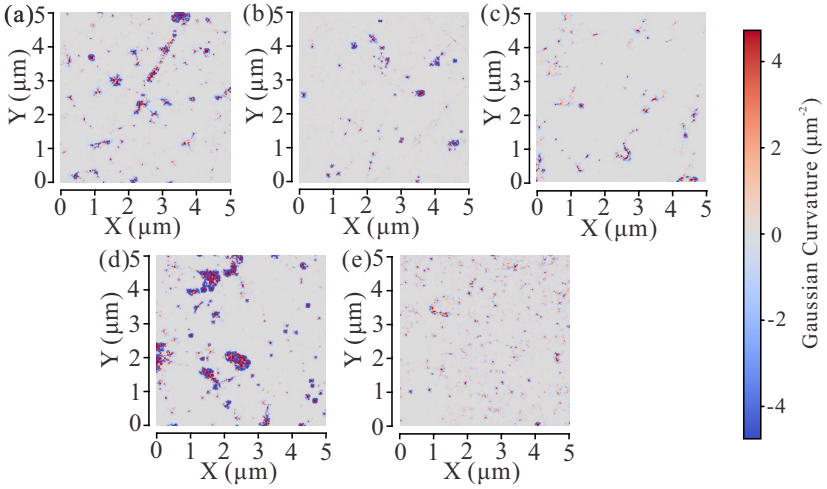

Fig. 6. Temperature-dependent evolution of sandstone surface characteristics: Gaussian curvature distributions at (a) 25 °C, (b) 200 °C, (c) 400 °C, (d)500 °C and (e) 700 °C.

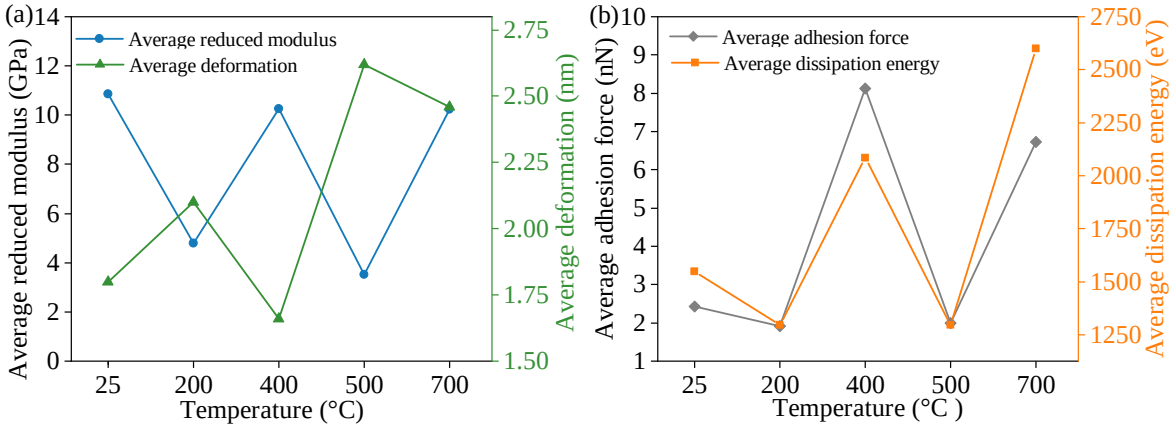

Fig. 7. Evolution of nanomechanical properties with temperature. (a) Average adhesion force and dissipation energy and (b) average reduced modulus and deformation.

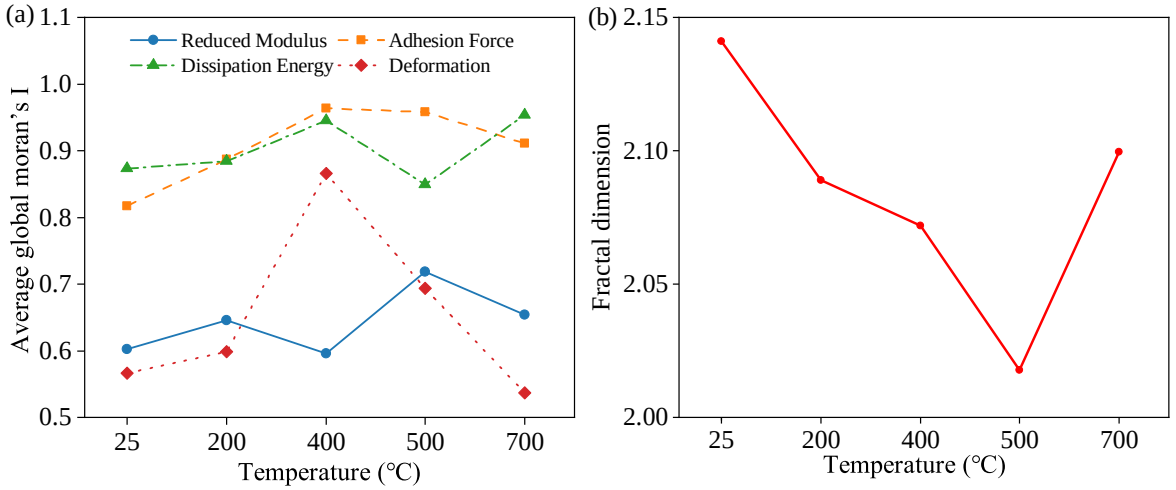

Fig. 8. Evolution of spatial autocorrelation and surface complexity with temperature. (a) Average Global Moran's Index and (b) average fractal dimension.

spherical-like curvature, while $K < 0$ indicates saddle-like curvature). In contrast, the Euler characteristic represents the overall topological connectivity of the surface by assessing the difference between the number of connected peak domains and the number of enclosed valley-holes in the binarized image (Fig. 5(b)).

3.3 Spatial distribution of nanomechanical properties at the key temperatures

Global and local spatial autocorrelation analyses were performed on four nanomechanical parameters of the heat-treated sandstone. At all tested temperatures, these parameters exhibited a statistically significant global positive spatial autocorrelation ($p < 0.001$). Fig. 7 illustrates the evolution of average nanomechanical properties with temperature. The core parameter of reduced modulus displayed a non-monotonic "degradation-recovery-degradation-recovery" trend: It decreased from 10.86 GPa at 25 °C to a minimum of 3.51 GPa at 500 °C, with notable recoveries to 10.26 GPa and 10.22 GPa at 400 and 700 °C, respectively. Concurrently, deformation peaked at 2.62 nm (at 500 °C), while the adhesion force reached its maximum of 8.12 nN at 400 °C. Dissipation energy recorded its process-wide minimum and maximum at 500 (1296.78 eV) and 700 °C (2600.36 eV), respectively.

In addition to the evolution of macroscopic average values, the spatial distribution pattern of each parameter also evolved significantly (Fig. 8(a)). The Global Moran's Index (I) for all parameters remained positive throughout the entire temperature range, indicating persistent spatial clustering. A clear trend of increasing spatial clustering was observed for most parameters up to 400 °C. For instance, Moran's I for adhesion force climbed from 0.817 at 25 °C to its peak of 0.964 at 400 °C (passing through 0.887 at 200 °C). Similarly, the indices for dissipation energy and deformation increased from their initial values of 0.873 and 0.566 at 25 °C to their respective peaks of 0.945 and 0.866 at 400 °C. In stark contrast, the reduced modulus exhibited a unique, non-monotonic evolution in its spatial clustering. Its Moran's I value increased from 0.602 (25 °C) to 0.646 (200 °C), dipped to 0.596 at 400 °C, and then surged to its maximum value of 0.718 at 500 °C before declining to 0.654 at 700 °C.

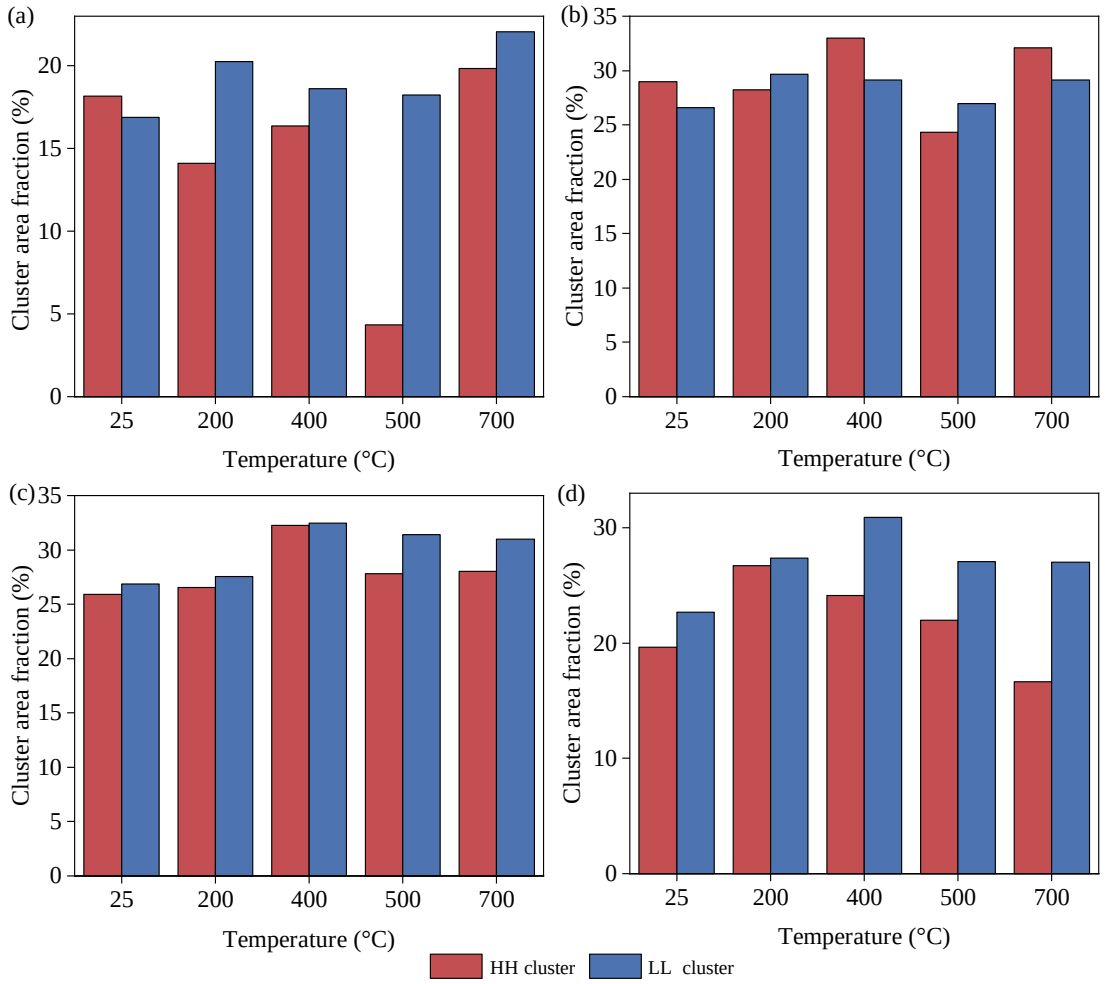

Fig. 9. Comparison of LISA clustering models with different mechanical parameters: (a) Reduced modulus, (b) dissipated energy, (c) adhesion force and (d) average cluster area proportions of HH and LL deformation.

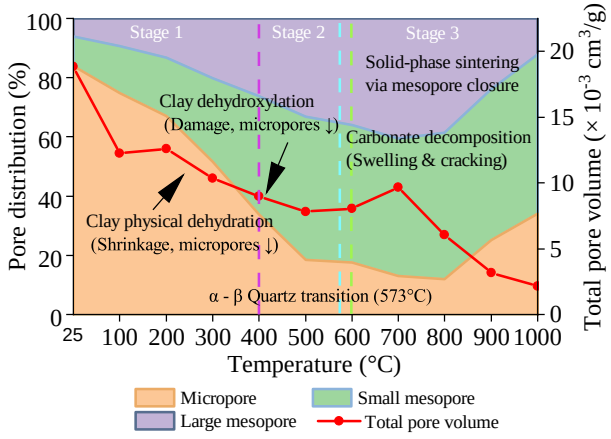

Fig. 10. Evolution of pore structure during heat treatment of sandstone.

The analysis of local clustering patterns (Fig. 9) reveals that the area fractions of High-High (HH) and Low-Low (LL) clusters for reduced modulus fluctuated significantly. At 25 °C, these fractions were 18.2% and 16.9%, respectively. By 200 °C, the area of LL clusters (20.2%) surpassed that of HH clusters (14.1%). Subsequently, the HH cluster area dropped to its process-wide minimum of 4.4% at 500 °C, while the LL cluster area remained at a relatively high level of 18.3%. For dissipation energy, the area fractions of HH and LL clusters remained closely matched throughout the entire heat treatment process, with both values peaking simultaneously at 400 °C (30.9% for HH and 30.7% for LL, respectively). In addition, the adhesion force exhibited a similarly balanced clustering characteristic, whereas deformation was consistently dominated by LL clusters.

4. Discussion

4.1 Pore system evolution mechanism

Through a systematic characterization in the range of 25 to 1,000 °C, this study aimed to reveal the complete evolutionary process of the sandstone pore system under continuous thermal perturbation and its underlying physicochemical mechanisms. The entire evolution could be divided into three stages dominated by different physicochemical processes (Fig. 10), which not only explains the observed changes in pore structure but also validates the rationale for focusing our in-depth analysis on the selected transition temperatures (25, 200, 400, 500, and 700 °C). In the first stage (25-400 °C), the evolution is

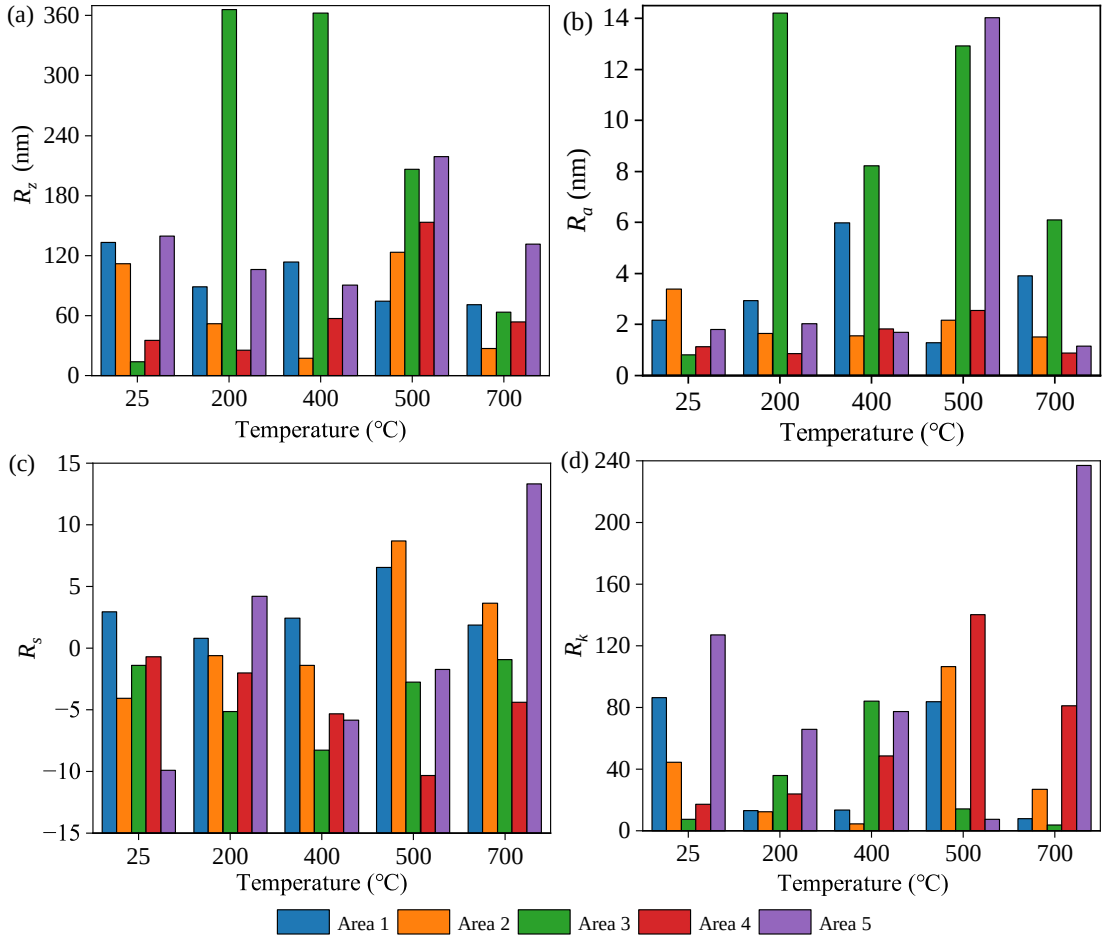

Fig. 11. Surface parameters of different regions of sandstone after heat treatment. (a) Maximum peak-to-valley height (R_z), (b) arithmetic mean roughness (R_a), (c) skewness (R_s) and (d) kurtosis (R_k).

governed by clay minerals: Physical dehydration around 200 °C causes shrinkage (Vigroux et al., 2021), while chemical dehydroxylation near 400 °C leads to its structural collapse (Guggenheim and Martin, 1995), with these two processes collectively resulting in a decrease in micropore volume and an increase in mesopores. The core mechanism of the second stage (400-600 °C) is the α-β phase transition of quartz ($\sim$ 573 °C). The immense local internal stresses induced by this transition (David et al., 1994), on the one hand, explain the reduction in total pore volume through compaction, while on the other hand, they maintain a high mesopore fraction by driving the formation of numerous thermally-induced microcracks (Glover et al., 1995). Therefore, 500 °C serves as a critical window for observing the transition from pore restructuring to microstructural damage. In the third stage ($>$ 600 °C), the sharp decline in pore volume is primarily attributed to the solid-phase sintering of minerals such as feldspar (Gautam et al., 2019). This process preferentially closes mesopores and densifies the structure, with its effect overpowering any potential pore creation from the concurrent decomposition of carbonate minerals (Rodriguez-Navarro et al., 2009).

4.2 Evolution of surface topography and damage

Taking the AFM analysis of sandstone at the key temperatures as a basis, this study quantitatively revealed the multi-stage evolution of its surface topography under thermal perturbation. In the initial-to-low temperature stage (25-200 °C), the evolution of surface topography was primarily characterized by a marked increase in damage heterogeneity. In the initial state at 25 °C, the sample itself already exhibited considerable natural variation, with a standard deviation for R_z (maximum height difference) of approximately 58.3 nm, while its Gaussian curvature distribution was relatively uniform (positive curvature: 41.85%; negative curvature: 58.15%). As the temperature was raised to 200 °C-a range known to induce the expulsion of pore water and the shrinkage of certain minerals (Zhang et al., 2016) – the experimental data reflected the non-uniform impact of these processes. At 200 °C, the standard deviation of R_z surged to $\sim$ 137.0 nm, far exceeding the initial dispersion, while the Gaussian curvature distribution showed more pronounced spatial heterogeneity (positive: 42.05%; negative: 57.95%). After treatment at 200 °C, one region of a sample exhibited an R_z value as high as 366.10 nm (the highest in the entire set) with a Gaussian curvature of 41.36% positive / 58.64% negative; in contrast, another

region had an R_z of only 25.19 nm (Fig. 11), indistinguishable from the initial state, with a Gaussian curvature of 42.51% positive / 57.49% negative. This indicates that in the low-temperature stage, thermal damage does not occur universally but is preferentially concentrated in certain intrinsically weak zones of the material.

As the heat treatment temperature reached the 400-500 °C range, the damage mode exhibited extreme and diverse characteristics. The experimental data showed a significant polarization in the distribution of surface skewness (R_s), with the coexistence of strongly negative regions ($R_s = -10.3193$ in region 500.4) and strongly positive regions ($R_s = +8.6799$ in region 500.2), indicating the simultaneous presence of both "deep-valley-dominated" (negative skewness zones) and "sharp-peak-dominated" (positive skewness zones) topographies. Concurrently, some sample regions displayed anomalous kurtosis values ($R_k > 80$)-with region 500.4 reaching as high as 140.12 and region 400.3 reaching 84.11-further confirming the intense surface heterogeneity. The Gaussian curvature distribution revealed a significant increase in the proportion of negative curvature (from 58.60% for the 400 °C group to 59.60% for the 500 °C group) and the appearance of extreme values, indicating that the polarization of local surface curvature continued to intensify. This topographical signature may be related to the differential thermal expansion among mineral grains, which triggers the large-scale extension and coalescence of intergranular microcrack networks, in turn forming pits from grain plucking (corresponding to negative curvature zones) and protrusions from grain compression (corresponding to high R_k zones) (Kranz, 1983; Hall, 1999; Gómez-Heras et al., 2006).

The test data indicate that, concomitant with the increase in macroscopic roughness parameters like Ra, the fractal dimension D reached its minimum at 500 °C (average value ≈ 2.01) (Fig. 8(b)). This negative correlation suggests that events dominated by large-scale surface fracture at this stage may have reduced the native surface complexity of the sandstone by removing or covering pre-existing features. As the temperature was raised further, the fractal dimension showed a recovery in some samples from the 700 °C group (reaching a high of 2.222), though with significant intra-regional variation (range of 0.117); its average value (2.100), however, remained below the initial state. This phenomenon is likely associated with the generation of new microcrack networks within the grains after the sample underwent the quartz α-β phase transition (573 °C) (Mahanta et al., 2020; Alcock et al., 2023). Correspondingly, the surface topography at 700 °C also displayed a new diversity; the Euler characteristic of some samples shifted from negative to positive, and "protrusion-dominated" samples with extremely positive skewness ($R_s = +13.30$) appeared, forming a sharp contrast with other "pit-dominated" regions within the same sample (Fig. 11). This may reflect more complex stress release and damage mechanisms at high temperatures.

4.3 Evolution of mechanical spatial distribution

This section discusses the results from the Global Moran's Index and Local Indicators of LISA analyses for each mechanical parameter. To systematically reveal the evolutionary regularities of its the spatial property distribution of heat-treated sandstone, a multi-level spatial autocorrelation analysis was conducted on the distribution of its micromechanical properties. The Global Moran's Index analysis, used to assess the overall strength of property clustering, confirmed that all mechanical parameters exhibited a statistically highly significant positive spatial autocorrelation ($p < 0.001$) under all test conditions. This indicates that the property distribution is not random but is inherently characterized by clustering phenomena. Building upon this finding, the LISA analysis further identified the specific types of clusters-namely, the "High-High" (HH, clustering of high-performance regions) and "Low-Low" (LL, clustering of low-performance/damaged regions) patterns-thereby providing critical evidence for the understanding of the underlying damage mechanisms.

In the initial and low-temperature stage (25-200 °C), damage initially manifests in a non-uniform and localized manner (Fig. 12). In terms of absolute mechanical properties, the material's overall stiffness undergoes a significant initial degradation; the group average of the reduced modulus decreased from ~ 10.86 GPa at 25 °C to ~ 4.79 GPa at 200 °C, a reduction of 61.4% (Fig. 7(b)). This degradation in macroscopic performance was mirrored by an increase in spatial clustering, as the average Global Moran's Index for the reduced modulus rose from 0.612 at 25 °C to 0.648 at 200 °C, with the absolute peak value ($I = 0.821$) for a single measurement area also occurring at 200 °C (Fig. 7(a)). The LISA analysis revealed the evolution of the internal composition: At 25 °C, the area fractions of high-stiffness and low-stiffness regions were still relatively balanced, whereas by 200 °C, the regional average of the LL area fraction (representing damaged zones), at approximately 20.26%, surpassed the HH fraction by 6.15 percentage points (Fig. 13). This indicates that the heightened clustering at this stage is primarily contributed by newly formed, contiguous low-stiffness regions, confirming that the initial thermal damage spatially manifests as the preferential expansion of weak zones.

The material exhibited a paradoxical mechanical rebound, initiating a critical stage of performance differentiation and reorganization at 400 °C. At this temperature, the material's stiffness underwent a mechanical rebound phenomenon: The group average of the reduced modulus recovered to 10.26 GPa, nominally approaching its initial state at 25 °C (Fig. 7). However, the Global Moran's Index analysis revealed that this phenomenon was not an overall improvement in performance, but rather the superficial manifestation of a complex structural reorganization. While the global clustering of the reduced modulus showed a decline, the spatial ordering of the other three mechanical parameters reached its peak for the entire evolutionary process (Fig. 12). The LISA analysis for dissipation energy provides a clear illustration: The combined area fraction of its high-value and low-value clusters reached an average of 62.148%, the maximum value across all temperatures, which visually illustrates that the polarization of the surface properties into high and low extremes had peaked (Fig. 13). Therefore, the stiffness recovery at 400 °C was in fact accompanied by a highly ordered and extreme spatial

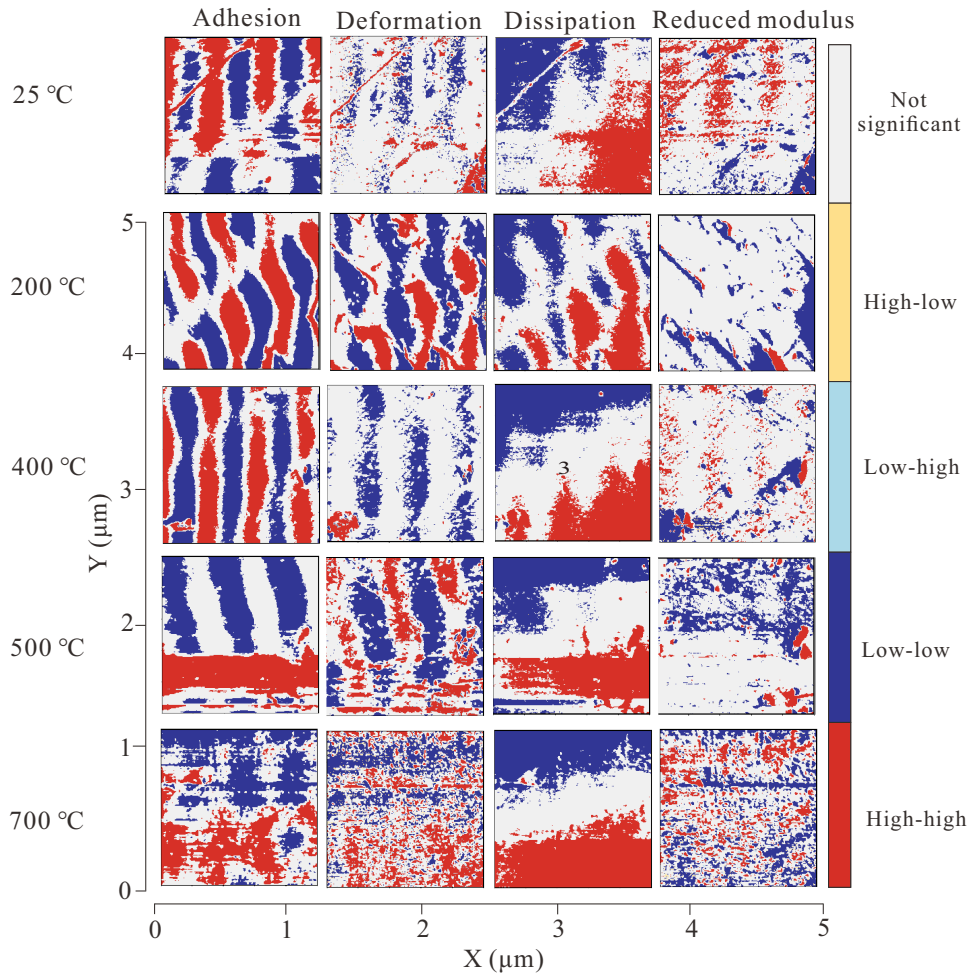

Fig. 12. Local Moran's *I* (LISA) maps for sandstone nanomechanical properties (adhesion force ,deformation, dissipation energy, and Reduced modulus) at 25, 200, 400, 500 and 700 °C.

distribution of the other mechanical properties.

In the mid-to-high temperature stage (500-700 °C), the spatial reorganization of stiffness became the dominant phenomenon. At 500 °C, a critical paradox emerged: The regional average of the Global Moran's Index for the reduced modulus reached its peak for the entire temperature range (average $I \approx 0.718$), yet this pinnacle of spatial clustering was accompanied by a severe degradation in the mechanical performance. Specifically, the average reduced modulus plummeted from ~ 10.26 GPa at 400 °C to ~ 3.50 GPa, a reduction of 66% (Fig. 9). The LISA analysis revealed the underlying mechanism of this paradox: At this stage, the area fraction of high-stiffness clusters sharply decreased to a mere 3.20%-5.70%, while the low-stiffness clusters maintained a high level of 15.54%-24.65% (Fig. 13). This stark contrast indicates that the strong global clustering at 500 °C was no longer a balanced coexistence of high- and low-performance zones, but instead was almost entirely dominated by a large-scale, nearly percolating low-stiffness damage network (the LL clusters) (Fig. 12). This damage-dominated structure exhibited stability at even higher temperatures. Upon reaching 700 °C, the LL area fraction remained at a high level (Fig. 13), suggesting that the sample had entered a final state in which it was severely damaged yet spatially stable.

From the perspective of the spatial heterogeneity of material stiffness, the coefficient of variation (CV) for the reduced modulus exhibited a clear evolutionary pattern with temperature. The calculation results showed that the CV reached its maximum value at 500 °C (with an average CV of ~ 84.5% across the five samples). This indicates that the stiffness distribution of the material was at its most non-uniform at this critical point, characterized by the coexistence of high-stiffness regions and low-stiffness damaged zones with stark differences, which is a direct manifestation of significant internal damage evolution. In contrast, the CV was at its minimum at 25 °C (average CV ≈ 21.4%), reflecting that the material possessed the highest degree of stiffness uniformity in its initial state, with a relatively intact internal structure (Fig. 14).

4.4 Topography-Mechanics coupling

This section employs bivariate LISA analysis to directly examine the spatial coupling relationship between the local elevation, as characterized by the AFM height maps, and the micromechanical parameters. The analysis will demonstrate the evolution of the spatial association patterns across different

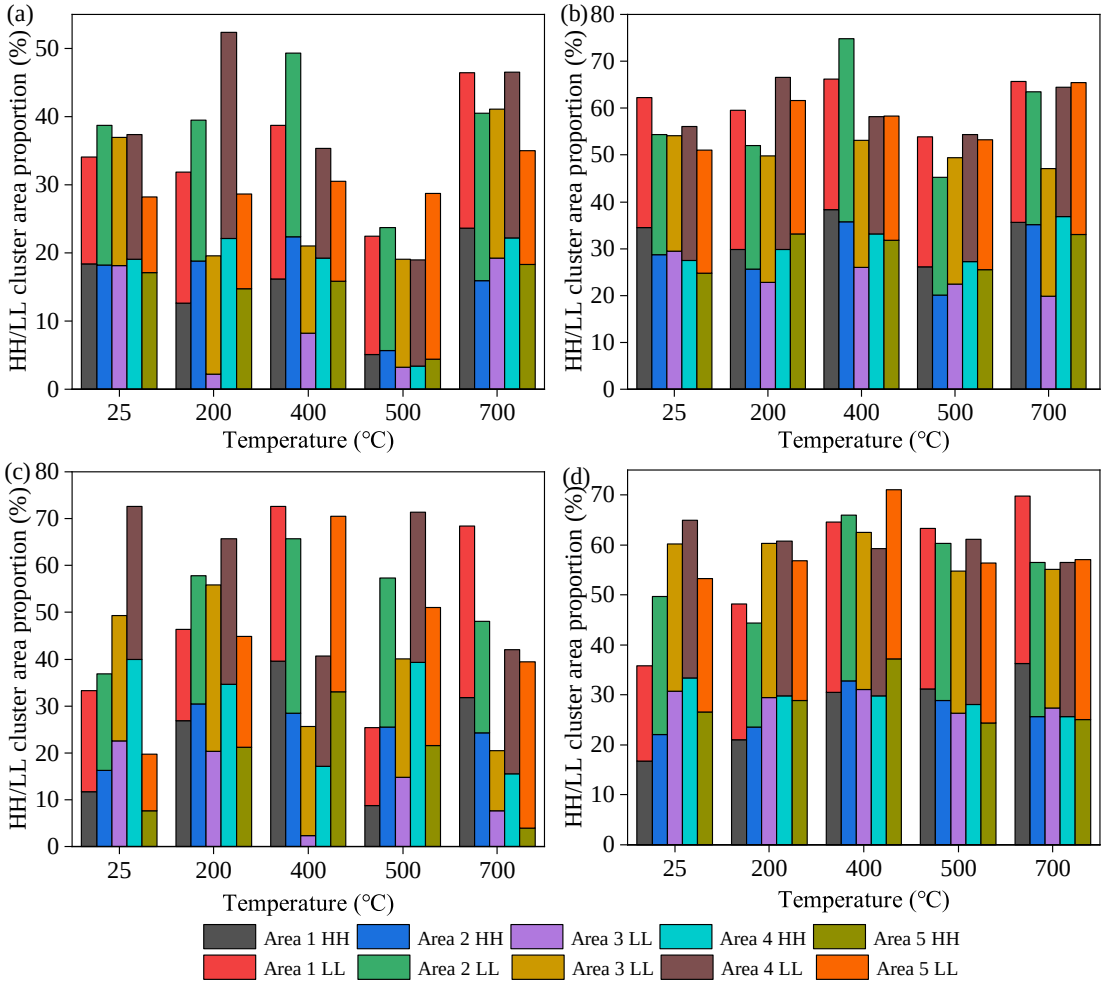

Fig. 13. Spatial clustering area proportion of surface mechanical properties of sandstone after heat treatment: (a) Reduced modulus, (b) dissipation energy, (c) deformation and (d) adhesion force.

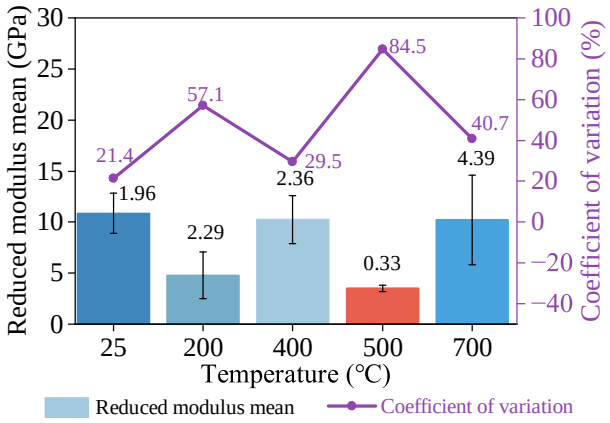

Fig. 14. Evolution of the mean reduced modulus and its CV with temperature.

temperature stages: 25, 200, 400, 500, and 700 °C.

At 25 °C, the sandstone surface already exhibited a topography-correlated mechanical heterogeneity: The reduced modulus of the highlands (15.1 GPa) was significantly higher than that of the troughs (9.0 GPa). After heat treatment at 200 °C, this non-uniformity was further amplified, leading to a non-uniform degradation concentrated in the trough regions. This degradation process is corroborated by multiple data points: The modulus in the troughs dropped sharply to 3.2 GPa, their spatial fraction increased from 14.1% to 21.7%, and their average deformation correspondingly rose from 1.8 to 2.2 nm (Fig. 15). Crucially, the energy dissipation in the trough regions underwent a sign reversal from positive to negative. This fundamental shift in surface interaction, combined with the material's macroscopic softening, indicates that the thermal treatment at 200 °C was not merely a simple degradation of physical properties but likely involved a more complex mechanism of surface alteration.

As the temperature was raised from 200 to 400 °C, the sandstone's mechanical response reversed its previous softening trend, exhibiting a significant hardening. The average modulus of the highlands recovered to 16.2 GPa, surpassing its initial value, while the deformation in the troughs dropped to its minimum point (0.49 nm). This enhancement in the macroscopic mechanical behavior, accompanied by surface interactions reaching their peak-with an adhesion force of 30.2 nN and energy dissipation of 4.43 keV (Fig. 14), collectively points to the formation of a dense, transient hardened structure

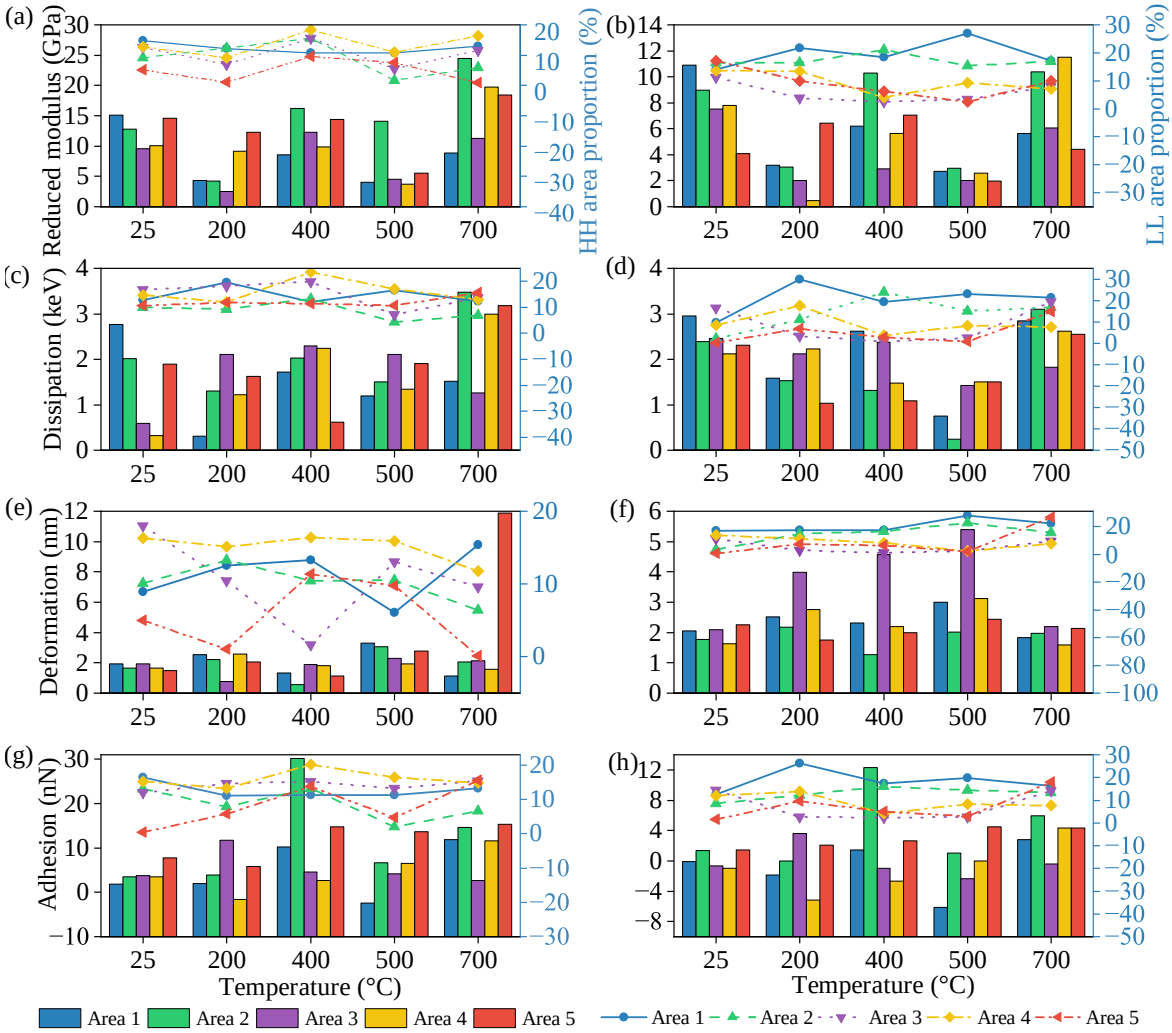

Fig. 15. Evolution of nanomechanical properties and area fractions within High-High (HH) and Low-Low (LL) clusters. (a)-(d) HH Clusters: (a) Reduced modulus and area fraction, (b) dissipation energy and area fraction, (c) deformation and area fraction and (d) adhesion force and area fraction. (e)-(h) LL Clusters: (e) Reduced modulus and area fraction, (f) dissipation energy and area fraction, (g) deformation and area fraction and (h) adhesion force and area fraction.

at 400 °C. However, this hardened state proved to be thermally unstable, undergoing a systematic degradation at 500 °C: The material's stiffness dropped to its minimum (trough modulus of 2.7 GPa), while the adhesion force systematically shifted to negative values (-6.2 nN) (Fig. 14). This transition from high adhesion to no adhesion provides strong evidence for the inference of thermal decomposition of the hardened phase formed at 400 °C. Therefore, the mechanical state at 500 °C was not a simple physical softening but rather the product of the thermal decomposition of the 400 °C transient structure, characterized by low stiffness and no adhesion.

After the degradation at 500 °C, the heat treatment at 700 °C led to a significant reconfiguration of the correlation between the mechanical properties and topography of the sandstone surface. In contrast to the "hard-highland, soft-trough" pattern of the initial state, a "high-modulus-in-trough" (High-Low clustering) pattern became significant at this stage (23.7% coverage) (Fig. 15). This indicates that under extreme high temperatures, the previously softer trough regions formed structures that were more rigid than some highland areas. This conclusion was independently verified by the deformation data, which showed that the "low-deformation-in-trough" pattern also occupied a significant spatial fraction (26.5%), confirming that the trough regions had acquired an enhanced resistance to deformation.

5. Conclusions

1) The pore system of sandstone undergoes a fundamental, staged transformation under thermal treatment: It evolves from an initially micropore-dominated structure to a final state governed by mesopores, with critical transition points of structural reorganization identified around 400 °C and a minimum in total porosity at 500 °C. This provides a clear basis for the targeted AFM analysis.
2) Quantitative AFM-based analysis reveals a multi-stage topographical evolution. The process shifts from an initial amplification of damage heterogeneity (up to 200 °C) to extreme topographical polarization in the 400-500 °C

range. This polarization, driven by large-scale fracturing, paradoxically results in a minimum in fine-scale fractal complexity. At 700 °C, the surface undergoes a fundamental reconfiguration, driven by new intragranular cracking, which partially restores its complexity and introduces novel damage signatures.

3) This study redefines thermal damage in sandstone as a mechanistic pathway, evolving from localized damage expansion, through a critical phase of transient hardening and extreme property polarization at 400 °C, to the formation of a dominant, interconnected damage network that drives the formation of peak heterogeneity at 500 °C. This demonstrates that the final mechanical state is a new, heterogeneous system whose properties are determined by its thermochemical history instead of its initial topography.
4) Bivariate LISA analysis reveals that the coupling between the topography and micromechanics of sandstone undergoes a multi-stage reorganization. The evolution progresses from an initial amplification of heterogeneity (200 °C), through the formation and subsequent decomposition of a transient hardened structure (400-500 °C), to a fundamental reconfiguration at 700 °C. The resulting "high-modulus-in-trough" pattern demonstrates that the final mechanical state is a new, heterogeneous system whose properties are determined by its local thermochemical history, superseding the influence of the initial topography.
5) The limitations of this study include 2D surface analysis, which overlooks 3D internal damage; ex-situ measurements that preclude real-time observation of dynamic processes; and a focus on a single rock type, limiting generalizability. Future work should integrate AFM with micro-CT for 3D correlative analysis, employ in-situ high-temperature techniques, and extend the framework to other lithologies to validate and broaden the findings.

Acknowledgements

This work was supported by the Science and Technology Research Program of Chongqing Municipal Education Commission (No. KJZD-K202401205), and the university-level research project of Chongqing Three Gorges University (No. YJSKY25042). We acknowledge the computational support provided by the Penn Institute for Computational Science (PICS) for the data processing and analysis.

Conflict of interest

The authors declare no competing interest.

References

Alcock, T., Bullen, D., Benson, P. M., et al. Temperature-driven micro-fracturing in granite: The interplay between microstructure, mineralogy and tensile strength. Heliyon, 2023, 9(3): e13871.

Anderson, A., Rezaie, B. Geothermal technology: Trends and potential role in a sustainable future. Applied Energy, 2019, 248: 18-34.

Anselin, L. Local indicators of spatial association-lisa. Geographical Analysis, 1995, 27(2): 93-115.

Barrett, E. P., Joyner, L. G., Halenda, P. P. The determination of pore volume and area distributions in porous substances. I. Computations from nitrogen isotherms. Journal of the American Chemical Society, 1951, 73(1): 373-380.

Chen, X, Tang, X, Zhang, R, et al. Changes in shale microstructure and fluid flow under high temperature: Experimental analysis and fluid-structure interaction simulation. Petroleum Science, 2025, 22(4): 1699-1711.

Chen, Y., Yu, Q., Zhu, Q. Experimental investigation and micromechanics-based damage modeling of the stress relaxation mechanical properties in gray sandstone. Computers and Geotechnics, 2022, 149: 104829.

Cliff, A. D., Ord, J. K. Spatial Autocorrelation. London, UK, Pion, 1973.

David, C., Wong, T., Zhu, W., et al. Laboratory measurement of compaction-induced permeability change in porous rocks: Implications for the generation and maintenance of pore pressure excess in the crust. Pure and Applied Geophysics, 1994, 143(1): 425-456.

Derjaguin, B. V., Muller, V. M., Toporov, Y. P. Effect of contact deformations on the adhesion of particles. Journal of Colloid and Interface Science, 1975, 53(2): 314-326.

Dubinin, M. M., Radushkevich, L. V. Equation of the characteristic curve of activated charcoal. Proceedings of the Academy of Sciences of the USSR, Physical Chemistry Section, 1947, 55: 331-333.

Gao, M., Yang, M., Lu, Y., et al. Mechanical characterization of uniaxial compression associated with lamination angles in shale. Advances Geo-Energy Research 2024: 13(1): 56-68.

Gauss, C. F. Disquisitiones Generales Circa Superficies Curvas. Göttingen, Germany, Dieterich, 1828.

Gautam, P. K., Verma, A. K., Singh, T. N., et al. Experimental investigations on the thermal properties of jalore granitic rocks for nuclear waste repository. Thermochimica Acta, 2019, 681: 178381.

Giergiel, M., Zapotoczny, B., Czyzynska-Cichon, I., et al. AFM image analysis of porous structures by means of neural networks. Biomedical Signal Processing and Control, 2022, 71: 103097.

Glover, P., Baud, P., Darot, M., et al. α/β phase transition in quartz monitored using acoustic emissions. Geophysical Journal International, 1995, 120(3): 775-782.

Gómez-Heras, M., Smith, B. J., Fort, R. Surface temperature differences between minerals in crystalline rocks: Implications for granular disaggregation of granites through thermal fatigue. Geomorphology, 2006, 78(3-4): 236-249.

Guggenheim, S., Martin, R. T. Definition of clay and clay mineral: Joint report of the AIPEA nomenclature and CMS nomenclature committees. Clays and Clay Minerals, 1995, 43(2): 255-256.

Guo, P., Bu, M., Zhang, P., et al. Mechanical properties and

crack propagation behavior of granite after high temperature treatment based on a thermo-mechanical grain-based model. Rock Mechanics and Rock Engineering, 2023, 56(9): 6411-6435.

Hall, K. The role of thermal stress fatigue in the breakdown of rock in cold regions. Geomorphology, 1999, 31(1-4): 47-63.

Haralick, R. M., Sternberg, S. R., Zhuang, X. Image analysis using mathematical morphology. IEEE Transactions on Pattern Analysis and Machine Intelligence, 1987, PAMI-9(4): 532-550.

He, F., Li, G., Kan, J., et al. Research progress on multi-scale damage of rock. Coal Science and Technology, 2024, 52(10): 33-53. (in Chinese)

Hirono, T., Lin, W., Nakashima, S. Pore space visualization of rocks using an atomic force microscope. International Journal of Rock Mechanics and Mining Sciences, 2006, 43(2): 317-320.

Kranz, R. L. Microcracks in rocks: A review. Tectonophysics, 1983, 100(1-3): 449-480.

Li, Y., Yang, J., Pan, Z., et al. Nanoscale pore structure and mechanical property analysis of coal: An insight combining AFM and SEM images. Fuel, 2019, 260: 116352.

Mahanta, B., Vishal, V., Ranjith, P., et al. An insight into pore-network models of high-temperature heat-treated sandstones using computed tomography. Journal of Natural Gas Science and Engineering, 2020, 77: 103227.

Mo, C., Zhao, J., Zhang, D. Real-time measurement of mechanical behavior of granite during heating-cooling cycle: A mineralogical perspective. Rock Mechanics and Rock Engineering, 2022, 55(7): 4403-4422.

Moran, P. A. P. Notes on continuous stochastic phenomena. Biometrika, 1950, 37(1-2): 17-23.

Paruchuri, A., Wang, Y., Gu, X., et al. Machine learning for analyzing atomic force microscopy (AFM) images generated from polymer blends. Digital Discovery, 2024, 3(12): 2533-2550.

Rodriguez-Navarro, C., Ruiz-Agudo, E., Luque, A., et al. Thermal decomposition of calcite: Mechanisms of formation and textural evolution of CaO nanocrystals. American Mineralogist, 2009, 94(4): 578-593.

Shen, M., Zhao, Y., Bi, J., et al. Micro-damage evolution and macro-mechanical property of preloaded sandstone subjected to high-temperature treatment based on NMR technique. Construction and Building Materials, 2023, 369: 130638.

Tian, X., Song, D., He, X., et al. A systematic review on the applications of atomic force microscopy for coal and rock characterization. Measurement, 2024, 232: 114722.

Vigroux, M., Eslami, J., Beaucour, A. L., et al. High temperature behaviour of various natural building stones. Construction and Building Materials, 2021, 272: 121629.

Wang, K., Du, G., Wang, G., et al. Using atomic force microscopy to study the morphological characteristics of clay minerals in dense sandstone reservoirs. Rock and Mineral Analysis, 2025, 44(2): 245-253. (in Chinese)

Wong, L. N. Y., Zhang, Y., Wu, Z. Rock strengthening or weakening upon heating in the mild temperature range? Engineering Geology, 2020, 272: 105619.

Wu, C., Zhu, H., Ju, Y., et al. CO_2 phase fluctuation-induced topological damage enhances shale strength. International Journal of Rock Mechanics and Mining Sciences, 2025, 194: 1365-1609.

Xie, H., Li, X. Microstructure and nanomechanical characterization of tectonic coal based on SEM, AFM, XRD and DSI. Surfaces and Interfaces, 2024, 46: 104158.

Zhang, W., Sun, Q., Hao, S., et al. Experimental study on the variation of physical and mechanical properties of rock after high temperature treatment. Applied Thermal Engineering, 2016, 98: 1297-1304.

Zhou, T., Yan, H., Zhou, X., et al. Temperature's impact on high-overmature shale's mechanical properties: Atomic force microscopy study. SPE Journal, 2025, 30(3): 1090-1104.

Zhu, H., Lu, Y., Pan, Y., et al. Nanoscale mineralogy and organic structure characterization of shales: Insights via afm-ir spectroscopy. Advances in Geo-Energy Research, 2024, 13(3): 231-236.